Electronic supplementary information

Fast oxygen ion migration in Cu–In–oxide bulk and its utilization for effective CO_2 conversion at lower temperature

Jun-Ichiro Makiura, Takuma Higo*, Yutaro Kurosawa, Kota Murakami, Shuhei Ogo, Hideaki Tsuneki, Yasushi Hashimoto, Yasushi Sato, Yasushi Sekine*

*Correspondence to: t-higo@aoni.waseda.jp, ysekine@waseda.jp

This file includes:

- Materials and Methods
- Supplementary text
- Figs. S1 to S24
- Tables S1 to S13
- Reference

Materials and Methods

Preparation of oxide powder

Using a complex polymerization method, $Cu_2In_2O_5$ and In_2O_3 powders were prepared. For them, $Cu(NO_3)_2 \cdot 3H_2O$ and $In(NO_3)_3 \cdot nH_2O$ (Kanto Chemical Co. Inc.) were used as precursors. After metal nitrates were dissolved in distilled water, excess citric acid and ethylene glycol (Kanto Chemical Co. Inc.) were added to the solution. The molar ratio of metal ion: citric acid: ethylene glycol was 1:3:3. The solution was dried and pre-calcined for 2 h at 673 K. After pre-calcination, the obtained powder was calcined for 10 h at 1123 K.

Using a wet-impregnation method, Cu-loaded In_2O_3 was prepared. First, In_2O_3 was soaked in 20 mL of distilled water. Next, it was stirred for 2 h using a rotary evaporator *in vacuo* at room temperature. Subsequently, $Cu(NO_3)_2 \cdot 3H_2O$ dissolved in 20 mL distilled water was added to the solution and was stirred again for 2 h under atmospheric pressure. After the solution was dried, the obtained sample powder was calcined at 773 K for 5 h.

Isothermal RWGS-CL cycle test

Isothermal RWGS-CL cycle testing was conducted using a thermogravimetric apparatus (TG-50A; Shimadzu Corp.). First, oxide powder filled in a sample pan was ramped up to pre-set temperatures (673, 723, 773, 823, 873 K) in Ar flow. Then, the oxide powder was reduced by 10 vol% H_2 balanced by Ar for 30 min (reduction step). After the reduction step, the reduced oxide was re-oxidized by 10% CO_2 (Ar balance) until no increase in the sample weight could be observed. A series of reduction and oxidation steps was defined as one cycle of isothermal RWGS-CL. The total flow rate was set constant to 100 mL min^{-1}. The amounts of reduction and oxidation (redox) were defined as the amounts of oxygen atoms released or restored in each step, as calculated using the following equation S1.

$$Amount\ of\ reduction\ or\ oxidation\ (redox)\ [mmol\ g^{-1}] = \frac{|\Delta m|}{m_{sample} \times M_O} \quad \text{(S1)}$$

In this equation, Δm / mg, m_{sample} / g and M_{O} / g mol^{-1} respectively represent the change of sample weight during each step, the initial sample weight, and molar mass of the oxygen atom. The average CO_2 splitting rate was defined as shown in equation S2.

$$Average\ CO_2\ splitting\ rate\ [\mu mol\ g^{-1}\ min^{-1}] = \frac{Amount\ of\ oxidation}{\Delta t} \times 10^3 \quad \text{(S2)}$$

Therein, Δt / min represents the time necessary to complete CO_2 oxidation. The differential reaction rate was also used for kinetic studies.

Temperature-programmed experiment

Temperature-programmed reduction by H_2 (H_2-TPR) was conducted using a thermogravimetric apparatus (TG-50A; Shimadzu Corp.) to evaluate the reduction properties of oxides. Oxide powder was heated from room temperature to 973 K in 10% H_2 flow at a ramping rate of 2 K min^{-1}.

Structural characterization for oxides

The specific surface areas were calculated from nitrogen adsorption isotherm at 77 K by the Brunauer−Emmett−Teller (BET) method (Gemini VII 2390a; Micromeritics Instrument). Powder X-ray diffraction (XRD) measurements were taken to elucidate the crystal structure of oxides using an X-ray diffractometer (Smart Lab-III; Rigaku Corp.) with Cu-$K\alpha$ radiation at 40 kV and 40 mA. Observation of the oxide particle morphology and the distribution of elements such as copper, indium, and oxygen were conducted using a scanning transmission electron microscope with an energy-dispersive X-ray spectrometer (STEM-EDX; HE-2200; Hitachi Ltd.). Furthermore, the calculation of the overlapping ratio between indium and copper was conducted using EDX images processed by Python. For image processing, each EDX-image of indium and copper was divided into square areas of pixels. Then each area was blurred and binarized. The indium ratio overlapping with Cu was calculated by dividing the copper existence area determined in the binarization by the Indium existence area also determined in the binarization. The copper ratio overlapping with indium was calculated similarly.

In-situ X-ray absorption fine structure

In-situ X-ray absorption fine structure (XAFS) analyses for In and Cu *K*-edge were conducted at the beamline BL07 of the SAGA Light Source. The $Cu_2In_2O_5$ powder was diluted by boron nitride (BN) and was pressed into a 10 mmϕ pellet. The pellet was attached to a cell for *in-situ* experiments. First, the sample pellet was ramped up to 523 K in N_2 flow and was pre-reduced by 10% H_2 (N_2 balance) for 60 min at 523 K. The XAFS spectra were measured during pre-reduction. After pre-reduction treatments, the pellet was ramped up to 773 K in N_2 flow. Then reduction by H_2 and oxidation by CO_2 of the pellet was conducted at 773 K. The XAFS spectra were measured in each treatment. The gas compositions were 10% H_2 (N_2 balance) at the reduction step and 10% CO_2 (N_2 balance) at the oxidation step. The total flow rate was set constant to 100 mL min^{-1} in the experiments. The obtained XAFS spectra were analyzed using software (Athena ver. 0.9.26).

X-ray photoelectron spectroscopy (XPS)

To obtain the data for the surface atomic ratio of Cu, In and O, XPS measurements were performed on Versa Probe II (Ulvac Phi Inc.) with Al Kα X-rays. Binding energies for each orbital were calibrated with C1s (284.8 eV). Oxides were treated by the following procedure using TG before XPS measurements. The oxides were reduced by 10vol% H_2 until the Cu-In alloy was fully formed, and then re-oxidized with 10 vol% CO_2. When various oxidation rates were reached, the atmosphere was switched to Ar flow for cooling. The oxidation rate was determined from the weight increase of the sample. Samples cooled to room temperature were removed and their XPS spectra were measured.

Supplementary text

The effect of BET surface area

BET surface areas of Cu-In_2O_3 are 4.5 m^2 g^{-1} for as-prepared sample ($Cu_2In_2O_5$), 3.2 m^2 g^{-1} after 1st cycle, and 0.8 m^2 g^{-1} after 3rd cycle (Table S2). As the cycle is repeated, the surface area tended to decrease. Regarding the results presented in Fig. S1 and Table S1, it is considered that the surface area affects CO_2 splitting rate more than the redox amount. In terms of comparisons with other OSMs, the surface area is not a critical factor for the higher performance of Cu-In_2O_3. For example, lanthanum-based perovskites [14] and Iron-Substituted Hexa-aluminates [19] are respectively 0.4–1.3 and 2–30 m^2 g^{-1}. Table S3 summarizes the CO_2 splitting rate and the BET surface area of Cu-In_2O_3 after RWGS-CL cycle tests at 773 K. Considering the data for Cu-In_2O_3 following trends are obtained; the specific surface area affects CO_2 splitting rate, and the higher the surface area, the higher splitting rate. However, on the other hand, CO_2 splitting rate per unit surface area is not constant, which demonstrates that CO_2 splitting rate is not monotonically dependent on the surface area. It is considered that the reason for this trend in Cu-In_2O_3 is that fast oxygen migration compensates for the reduction of active sites due to the low specific surface area.

EDX map processing and analysis for Cu-In_2O_3 during RWGS-CL

In order to estimate the Indium ratio overlapping with Copper in the STEM-EDX images, image analysis of EDX maps (Fig. S4B) was conducted after processing the images by python3. In the processing, EDX map images of Copper and Indium were first blurred and binarized as shown in Fig. S5. Blurring and binarizing were conducted with the help of CV2 library in OpenCV. The function used in the blurring is as follows.

```
blurred_image = cv2.GaussianBlur(image, (5, 5), 0)
```

Arguments passed to the cv2. GaussianBlur function are the original EDX-mapping image (image), gaussian kernel size (5,5) and the standard deviation of x axis (0 of automation) respectively. The function used in the binarizing is as follows.

```
threshold, binarized_image = cv2.threshold(blurred_image, 5, 255, cv2.THRESH_BINARY)
```

Arguments passed to the cv2.threshold function are the blurred image (blurred image), threshold (5), binarizing value for the pixel surpassed threshold (255) and the method of binarizing (cv2.THRESH_BINARY) respectively. And finally, the Indium ratio overlapping with Copper was estimated using the following calculation, with the help of NumPy library represented as np.

```
In_ratio=np.count_nonzero(Cu_binarized_image==255)/np.count_nonzero(In_binarized_image == 255)
```

The Copper ratio overlapping with Indium was estimated in the same way.

In addition, Indium (Copper) ratio overlapping with Copper (Indium) in the STEM-EDX of 10wt% Cu/In_2O_3 (Figs. S12 and S13) was estimated in the same manner as Cu-In_2O_3.

In-situ XAFS measurements

To investigate more details of the redox mechanism of Cu-In_2O_3, *in-situ* XAFS measurements were conducted. The measurement procedure is shown in the method section. First, the Cu *K*-edge and In *K*-edge XANES spectra of Cu-In_2O_3 during pre-reduction are presented respectively in Figs. S6 and S7. The spectra of Cu *K*-edge and In *K*-edge for as-prepared $Cu_2In_2O_5$ were, respectively, similar to those of CuO and In_2O_3. The valence of In and Cu in $Cu_2In_2O_5$ were considered to be In(III) and Cu(II). By pre-reduction, the spectrum of Cu *K*-edge changed to a similar spectrum to that of Cu-foil, whereas the spectrum of In *K*-edge changed only slightly. These results demonstrate that only the reduction of Cu(II) in $Cu_2In_2O_5$ to Cu(0) proceeded. Fig. S8 presents XANES spectra of In *K*-edge (panels A and B) and Cu *K*-edge (panels C and D) during RWGS-CL cycle at 773 K. The degree of reduction of In during RWGS-CL was estimated using a linear combination fitting (LCF) analysis (Table S4). The reduction of Cu-In_2O_3 proceeds by 49.3% in 30 min. Moreover, the oxidation was almost completed in 60 min, which agrees well with cycle-reaction test results. Characteristic XANES spectra of Cu *K*-edge were observed during H_2 reduction at 773 K. The spectra do not correspond to those of Cu-foil, CuO, and Cu_2O as standard samples. They cannot be replicated by a linear combination of these standard samples. For the spectra, the peak intensity assigned to the 1s to 4p transition decreased compared to that for the Cu-foil spectrum, which indicates that Cu metallic atoms interact with other metallic atoms. The electron of In atoms was probably transferred to metallic Cu atoms because of the difference of electronegativity between Cu and In. Similar features of XANES spectra were described in earlier reports of bimetallic compounds such as Sn@Cu core–shell nanoparticles [22,23]. The formation of Cu-In alloy was also confirmed from these *in-situ* XAFS measurements. During the oxidation step, this characteristic spectrum for Cu only slightly changed for 30 min, which demonstrates that the In oxidation proceeds while most of the Cu retains its interaction with the un-oxidized In, which is consistent with the oxidation mechanism inferred from the reaction model fitting, which mentioned later.

Structural characterization of 10wt% Cu/In_2O_3

Fig. S9 shows the performance of Cu/In_2O_3 for RWGS-CL at 773 K. As the amount of Cu loading increases, the amount of redox tends to increase. On the other hand, CO_2 splitting rate of more than 20wt%Cu-loaded In_2O_3 was much lower than that of pure In_2O_3. From these results, 10wt% Cu/In_2O_3 was determined as the most suitable control material.

The structural information (powder XRD and STEM-EDX) for 10wt% Cu/In_2O_3 is presented in Figs. S10–S12. As these results show, the RWGS-CL cycle on 10wt% Cu/In_2O_3 is based on the redox of indium with the formation and re-oxidation of Cu-In alloy, as in the case of Cu-In_2O_3. As a result of the image processing and analysis for these EDX images (Fig. S13), although 98% of Cu exists overlapping with In, only 57% of In present in the field overlapped with Cu after reduction. This fact indicates that the large Cu particle migrated to the surface of In_2O_3 during oxidation and ended up losing sufficient contact with In_2O_3.

Temperature-programmed reduction by H_2 (H_2-TPR)

Temperature-programmed reduction by H_2 (H_2-TPR) measurements was conducted to investigate the reducibility of oxides (Cu-In_2O_3, 10wt% Cu/In_2O_3 and pure In_2O_3 without Cu loading), the results of which are presented in Fig. 5A. The reduction of In_2O_3 occurred at temperatures higher than 700 K. This finding agrees with earlier reports of the literature for In_2O_3 catalysts [32]. In the case of Cu-containing oxides (Cu-In_2O_3 and 10wt% Cu/In_2O_3), the H_2-TPR profiles showed three notable reduction areas (about 400–550 K, 580–700 K, and 700–920 K). The H_2-TPR behavior of Cu-In_2O_3 from $Cu_2In_2O_5$ can be represented by the following equations S3–S5.

$$Cu_2In_2O_5 \ + \ 2\,H_2 \rightarrow Cu_2 - In_2O_3 \ + \ 2\,H_2O \tag{S3}$$

$$Cu_2 - In_2O_3 \ + \ 1.3\,H_2 \rightarrow Cu_2In_{0.87} - In_{1.13}O_{1.7} \ + \ 1.3\,H_2O \tag{S4}$$

$$Cu_2In_{0.87} - In_{1.13}O_{1.7} \ + \ 1.7\,H_2 \rightarrow Cu_2In_{0.87} - In_{1.13}(metal) \ + \ 1.7\,H_2 \tag{S5}$$

Reduction in the low-temperature region of 400–550 K (equation S3) was the reduction of Cu(II) to Cu(0). In the moderate temperature region of 580–700 K, the amount of reduction was equivalent to about 26% of oxygen contained in $Cu_2In_2O_5$. Therefore, the reduction of In(III) with the formation of Cu-In alloy, the composition of which finally reached near Cu_9In_4, was considered to proceed in this moderate temperature region (equation S4). Then, the remaining indium oxide was simply reduced in the high-temperature region as shown in equation S5. For 10 wt% Cu/In_2O_3, the reduction steps are similar to that of Cu-In_2O_3 because the H_2-TPR profile shows three reduction regions.

Reaction kinetic models

In order to investigate the mechanism of isothermal solid-state reaction in the RWGS-CL condition, the reaction kinetic study was conducted. In this study, the method which Hancock and Sharp proposed to distinguish reaction mechanisms [25], was applied. The following equation S6 derives from Avrami-Erofe'ev equation [28–30] which is based on the classical nucleation and grain growth model.

$$\ln\left(-\ln\left(1-x\right)\right) = \ln\left(a\right) + n\ln\left(t\right) \tag{S6}$$

where x is the fraction reacted in time *t* (: the solid conversion), a is the constant based on the frequency of the nuclei formation and the rate of grain growth, and n is the constant associated with the geometry of the system.

In this method, the plots of ln(−ln(1−*x*) *vs*. ln(*t*) is used to infer a suitable model for the reaction focused on. Table S5 shows rate equations and n values for various solid-state reaction models. Besides the nucleation model, the Phase-boundary-controlled reaction model which is categorized as the shrinking core model, the reaction order model and the diffusion model; these are typical reaction models for isothermal solid-phase reactions. Hancock and Sharp proposed that linear plots are obtained for these models as well, if the conversion *x* is limited to the range of 0.15–0.5. Therefore, it is possible to verify the kinetic model by the value of slope *n* obtained from the plots, and this method has been employed in previous literatures for Chemical-looping process [26,27].

Model fitting for the reduction of oxides

In this study, the experimental data of the reduction by H_2 was obtained by a thermogravimetry. The conversion of the reduction is defined as the following equation S7.

$$x(reduction) = \frac{m_i - m_t}{m_i - m_f} \quad (S7)$$

where m_i is the initial weight, m_t is the weight at a time and m_f is the final weight of oxides. For pure In_2O_3, m_f is defined as the weight when completely reduced to In metal. On the other hand, for Cu containing oxides (Cu-In_2O_3 and 10wt% Cu/In_2O_3), m_f is defined as the weight at the end of Cu-In alloy formation, in order to investigate the kinetic model for the reduction with the formation of Cu-In alloy. Fig. S14 presents the plots of $\ln(-\ln(1-x))$ vs. $\ln(t)$ for the reduction of oxides by H_2. Since the average n values were 1.038–1.074, AE1, R2 and R3 models were adopted as the candidates for a suitable model. The experimental and calculated conversion are shown in Figs. S15–S17. The phase-boundary-controlled reaction models (R2 and R3) seemed to fit relatively well with the experimental data. Comparing the experimental data and the calculated conversion, root-mean square deviation (RMSD) was investigated and presented in Tables S6–S8. The models with smaller RMSD values were determined as a suitable model.

Model fitting for the oxidation of reduced oxides

In this study, the experimental data for the oxidation by CO_2 was obtained by a thermogravimetry. The conversion of the oxidation step is defined as the following equation S8.

$$x(oxidation) = \frac{m_f - m_t}{m_f - m_i} \quad (S8)$$

where m_i is the initial weight, m_t is the weight at a time and m_f is the final weight of oxides. Pre-reduction by H_2 was conducted for all the oxides. For the Cu containing oxides (Cu-In_2O_3 and 10wt% Cu/In_2O_3), pre-reduction was conducted until the Cu-In alloy formation finished, in order to investigate the kinetic model for the oxidation of Cu-In alloy. Fig. S18 presents the plots of $\ln(-\ln(1-x))$ vs. $\ln(t)$ for the oxidation of the reduced oxides. Since the average n values were 0.832–1.218, AE1, R1, R2 and R3 models were adopted as the candidates for a suitable model. The experimental and calculated conversion are shown in Figs. S19–S21. As for Cu-In_2O_3, the Zero-order reaction model (R1) shows good fitting, although the gap is bigger between the calculation and the experimental data as the conversion increased higher than 0.7–0.8 (Fig. S19 and table S10). Thus, most of the oxidation proceeds according to the R1 model, and the rate-determining step is considered to be changed in the high conversion region. For the other two oxides, the most suitable model is determined as AE1 model (Figs. S20, S21 and tables S11, S12).

XPS measurements

XPS spectra of $Cu2p_{3/2}$ and $In3d_{5/2}$ for Cu-In_2O_3, which are at various re-oxidation rates are shown in Fig. S22. The spectrum labeled 0% indicates that of Cu-In_2O_3 forming In-Cu alloy after reduction treatment, while that labeled 100% indicates that of Cu-In_2O_3 after fully re-oxidized by CO_2. Almost identical spectra of Cu were obtained for Cu-In_2O_3 with re-oxidation rate of 0–90 %. Cu species on the surface had the metallic Cu(0) state [31,33]. Weak satellite peaks appeared on the spectrum when re-oxidation rate reached 100%, indicating that the surface Cu species is close to Cu(I)[33]. These results indicate Cu species on Cu-In_2O_3 during RWGS-CL cycle is almost metallic Cu, which agrees well with the results of XANES measurements. With respect to the shape of spectra of $In3d_{5/2}$, there was less difference between each re-oxidization rate. These spectra contain In(0) and In(III) components [31, 33]. Only the spectrum labeled as 100% is slightly shifted to the higher binding energy, which indicates an increase in the ratio of In(III). However, it is difficult to reasonably separate these $In3d_{5/2}$ spectra into two components. Therefore, in this study, the surface composition ratio of Indium and Oxygen obtained from XPS measurements was calculated in order to investigate the reduced state for the surface of Cu-In_2O_3 and 10wt% Cu/In_2O_3 during the re-oxidation step.

Additional Investigation of other alloy-oxide complex material

In terms of cost-effectiveness for OSMs, as additional investigation, the potential of substitution or reduction of Indium was investigated.

CuO-SnO_2 complex oxide was prepared by a complex polymerization method, then the RWGS-CL cycle test was conducted at 773 K whose results are presented in Fig. 23. CuO-SnO_2 was not re-oxidized under 10%CO_2 atmosphere (Fig. 23A). The XRD pattern of CuO-SnO_2 after the cycle test showed the formation of $Cu_{3.02}Sn_{0.98}$ alloy (Fig. 23B). These results demonstrate that, at least under the RWGS-CL condition we focus on, CO_2 splitting hardly proceeds over Cu-Sn alloy.

CuO-In_2O_3 complex oxide with the molar ratio of Cu/In = 2 as In–Cu–oxide bulk material and conducted RWGS-CL cycle test at 773 K. Fig. 24A shows the performance of CuO-In_2O_3 (Cu/In = 2). The performance of CuO-In_2O_3 (Cu/In = 2) was slightly inferior to that of Cu-In_2O_3 (Cu/In = 1). Dependence of differential CO_2 splitting rate on the conversion of oxides is presented in Fig. 24B. On CuO-In_2O_3 (Cu/In = 2), as in the case of Cu-In_2O_3 (Cu/In = 1), CO_2 splitting proceeded without a sharp decrease in rate, which suggests that oxygen ion migration was relatively fast. Therefore, the design of In-Cu-oxide bulk material has potential, especially in terms of cost-effectiveness.

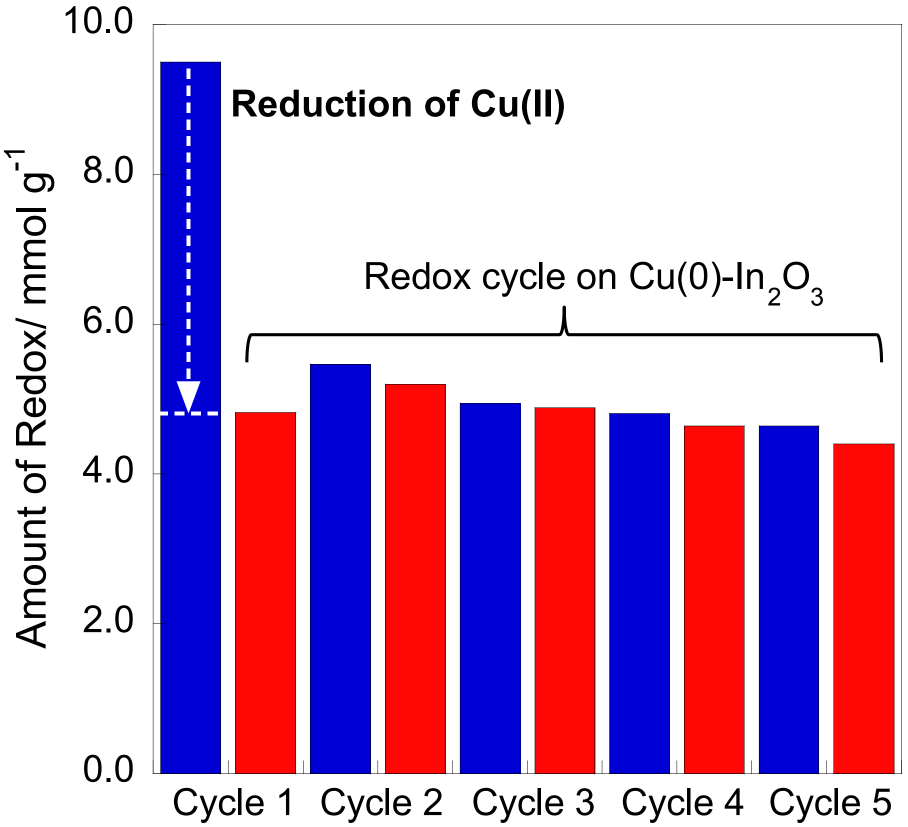

Fig. S1.

Isothermal RWGS-CL performance on $Cu_2In_2O_5$ at 773 K. Bars represent the amount of reduction (blue bars) and oxidation (red bars).

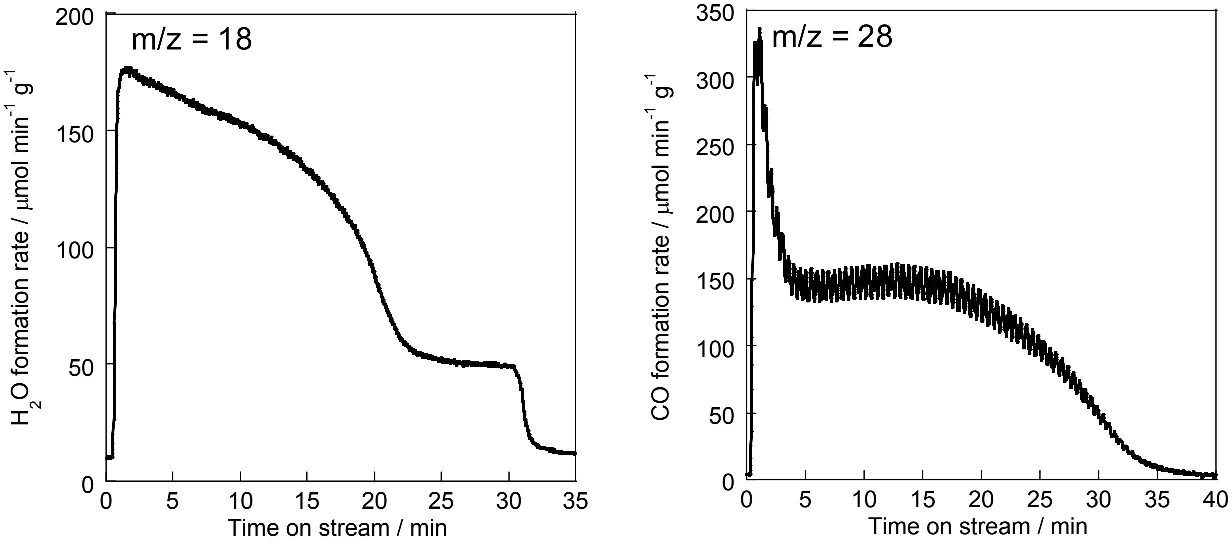

Fig. S2.

H_2O and CO formation during isothermal RWGS-CL on $Cu_2In_2O_5$ at 773 K.

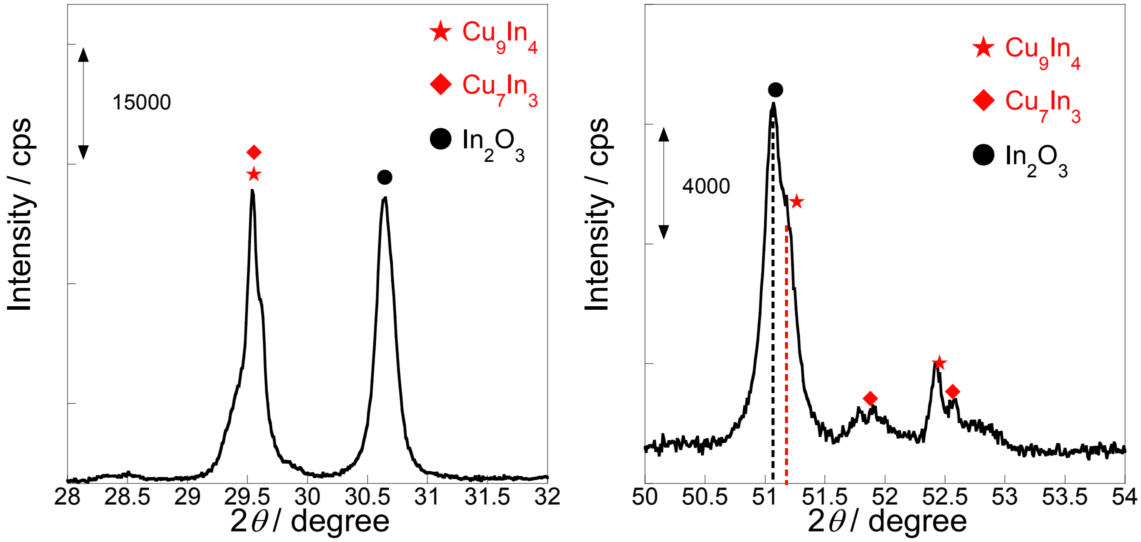

Fig. S3.

Characteristic diffraction peaks of Cu-In_2O_3 after H_2 reduction.

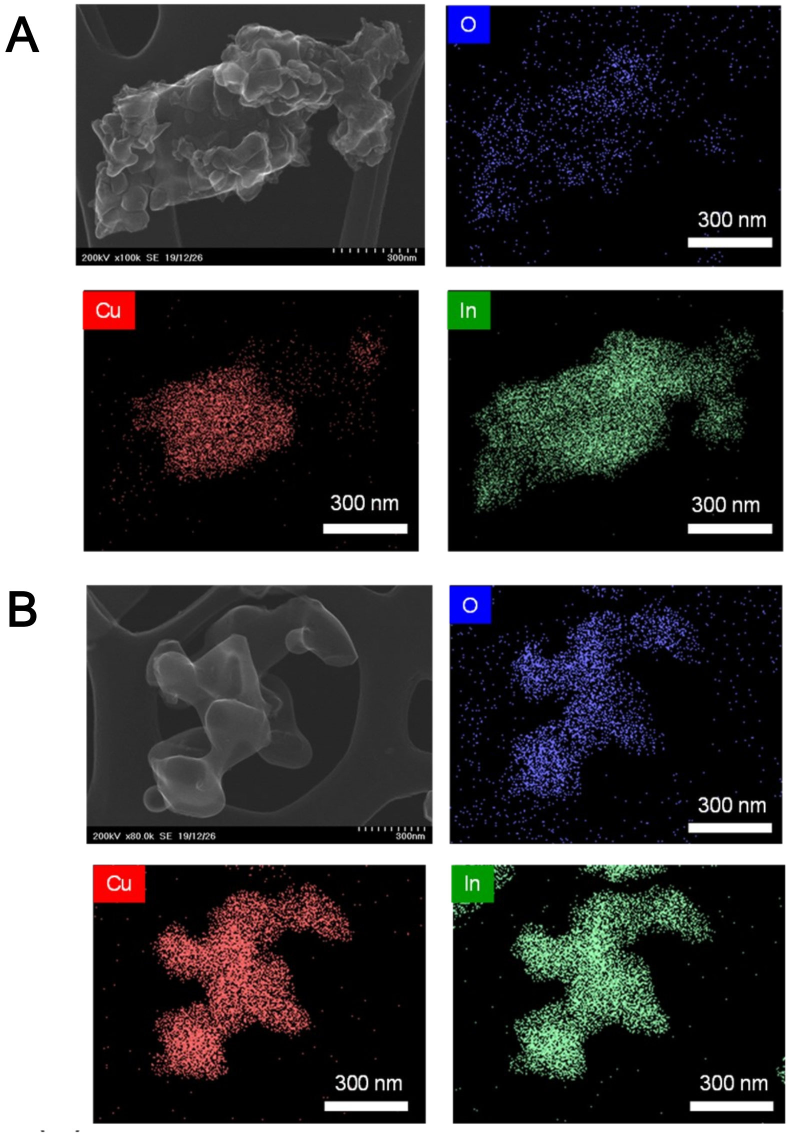

Fig. S4.

STEM-EDX images of Cu-In_2O_3 after RWGS-CL cycle. STEM-EDX images for $Cu_2In_2O_5$ (A) after reduction at 773 K and (B) after oxidation at 773 K (copper – red; indium – green; oxygen – blue).

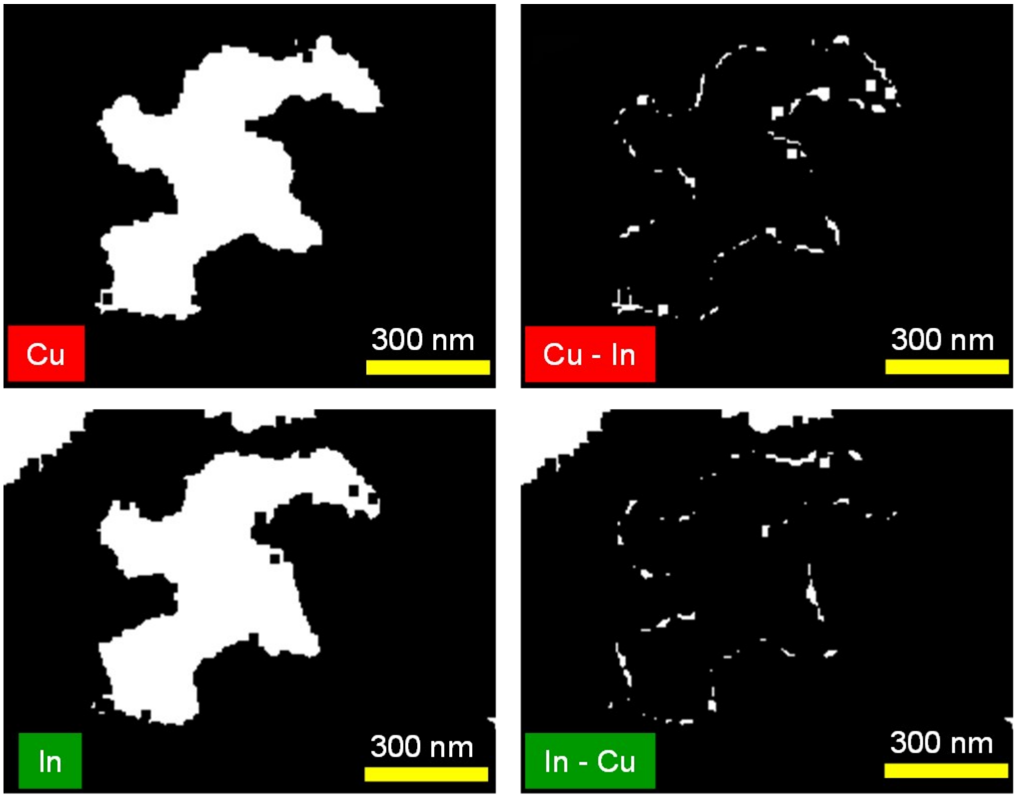

Fig. S5.

Binarized EDX mapping images for Cu-In_2O_3 after oxidation at 773 K.

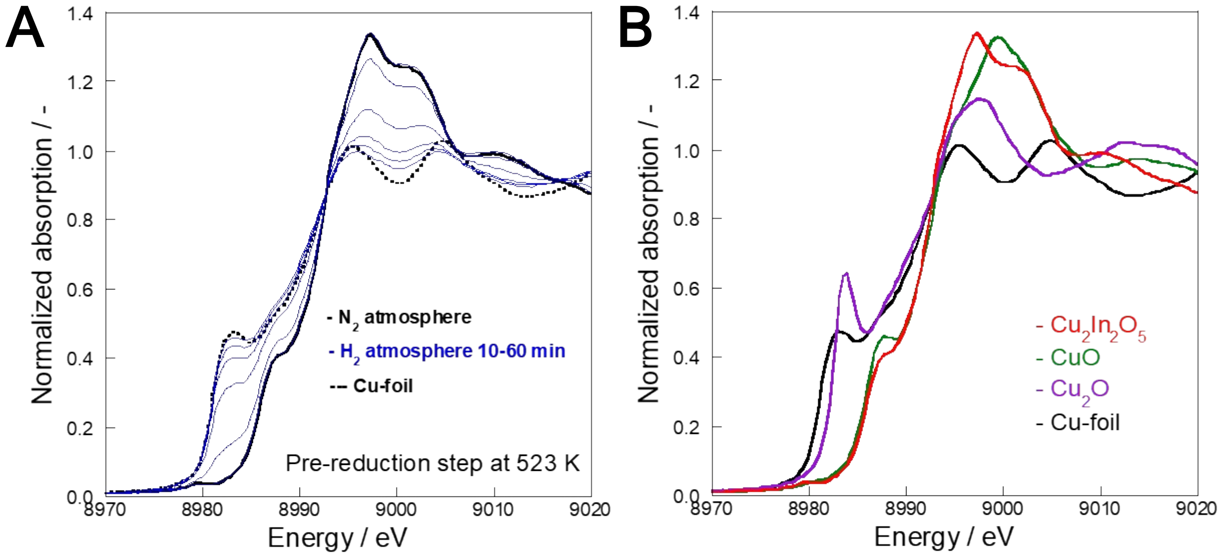

Fig. S6.

Cu *K*-edge XANES spectra for $Cu_2In_2O_5$ during pre-reduction at 523 K. (A) Sequential change of Cu *K*-edge XANES spectrum for $Cu_2In_2O_5$ during pre-reduction at 523 K. (B) The comparison of XANES spectrum for prepared $Cu_2In_2O_5$ with that for standard samples (CuO, Cu_2O and Cu-foil).

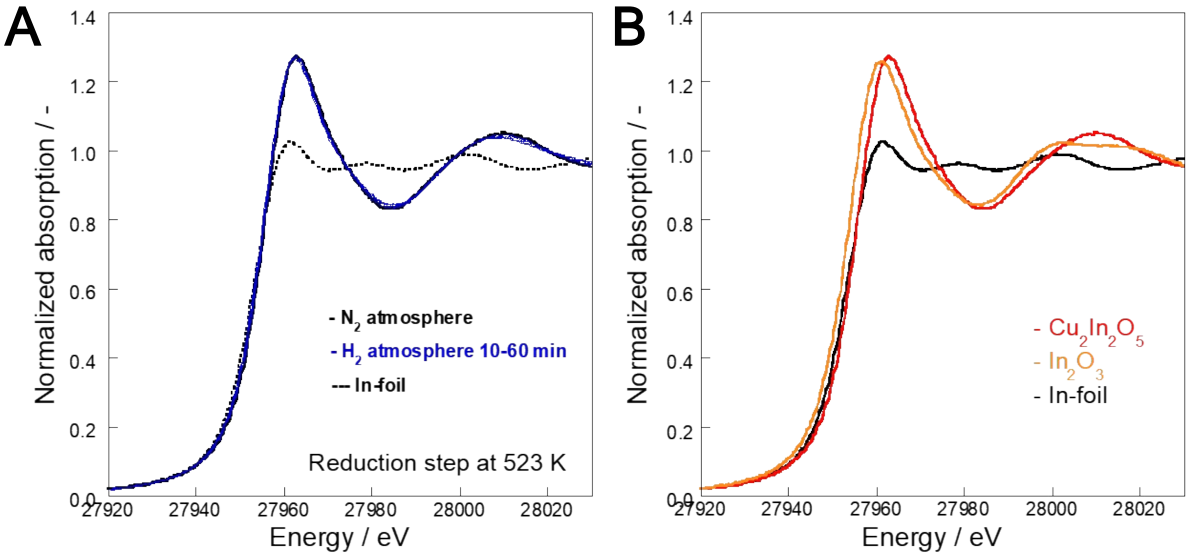

Fig. S.7

In *K*-edge XANES spectra for $Cu_2In_2O_5$ during pre-reduction at 523 K. (A) Sequential change of In *K*-edge XANES spectrum for $Cu_2In_2O_5$ during pre-reduction at 523 K. (B) The comparison of XANES spectrum for prepared $Cu_2In_2O_5$ with that for standard samples (In_2O_3 and In-foil).

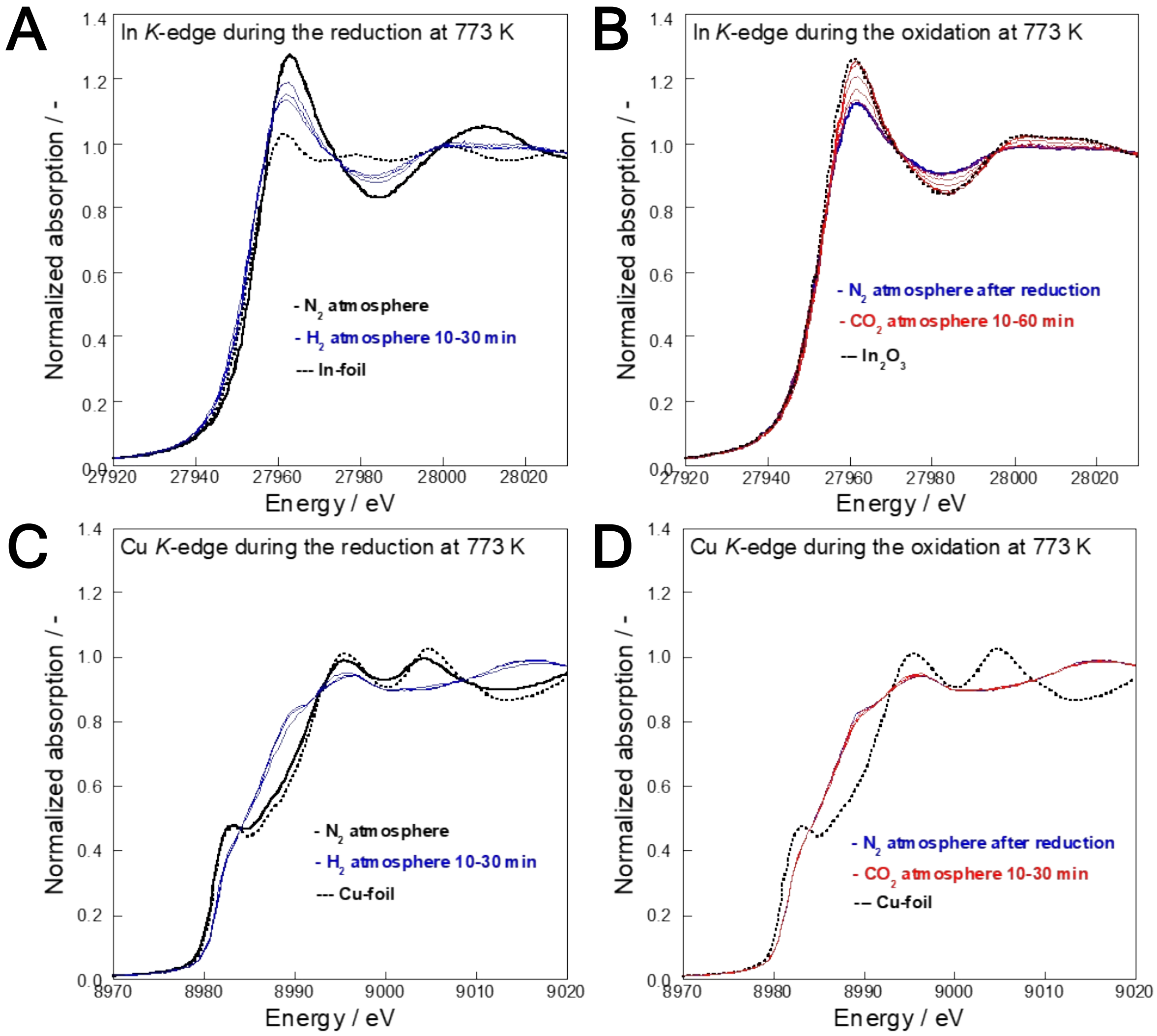

Fig. S8.

XANES spectra for Cu-In_2O_3 during RWGS-CL cycle at 773 K. In *K*-edge XANES spectra of Cu-In_2O_3 during reduction (A) and re-oxidation (B). Cu *K*-edge XANES spectra of Cu-In_2O_3 during reduction (C) and re-oxidation (D).

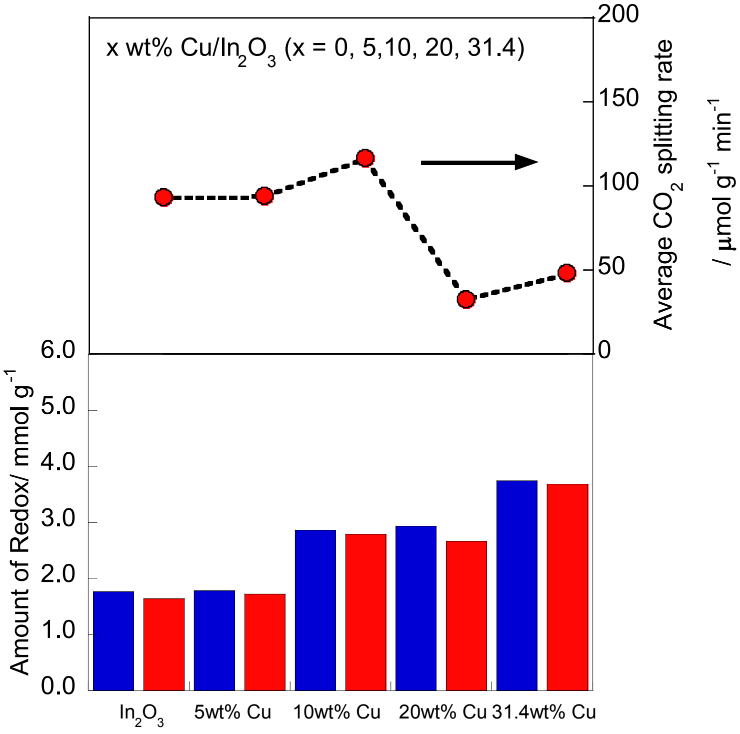

Fig. S9.

Amounts of redox and average CO_2 splitting during re-oxidation step on x wt% Cu/In_2O_3 (x = 0, 5, 10, 20, 31.4) for RWGS-CL at 773 K. Bars represent the amount of reduction (blue bars) and oxidation (red bars).

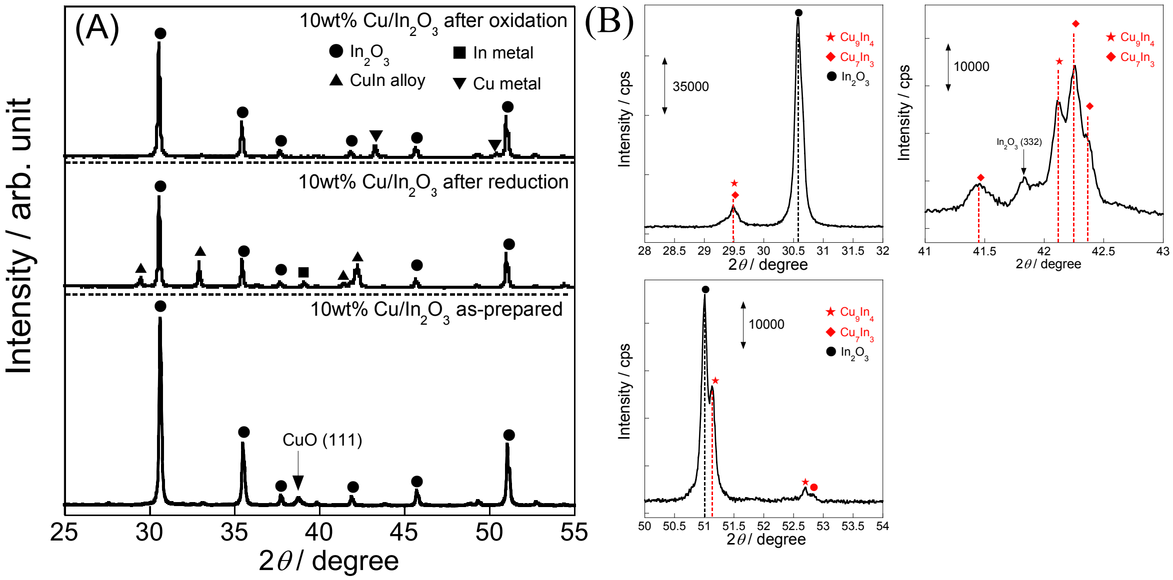

Fig. S10.

XRD diffraction patterns of 10wt% Cu/In$_2$O$_3$. (A) XRD profiles of 10wt% Cu/In$_2$O$_3$ as prepared, after reduction and after re-oxidation. (B) Main diffraction peaks for In-Cu alloy in the XRD profile of 10wt% Cu/In$_2$O$_3$ after reduction.

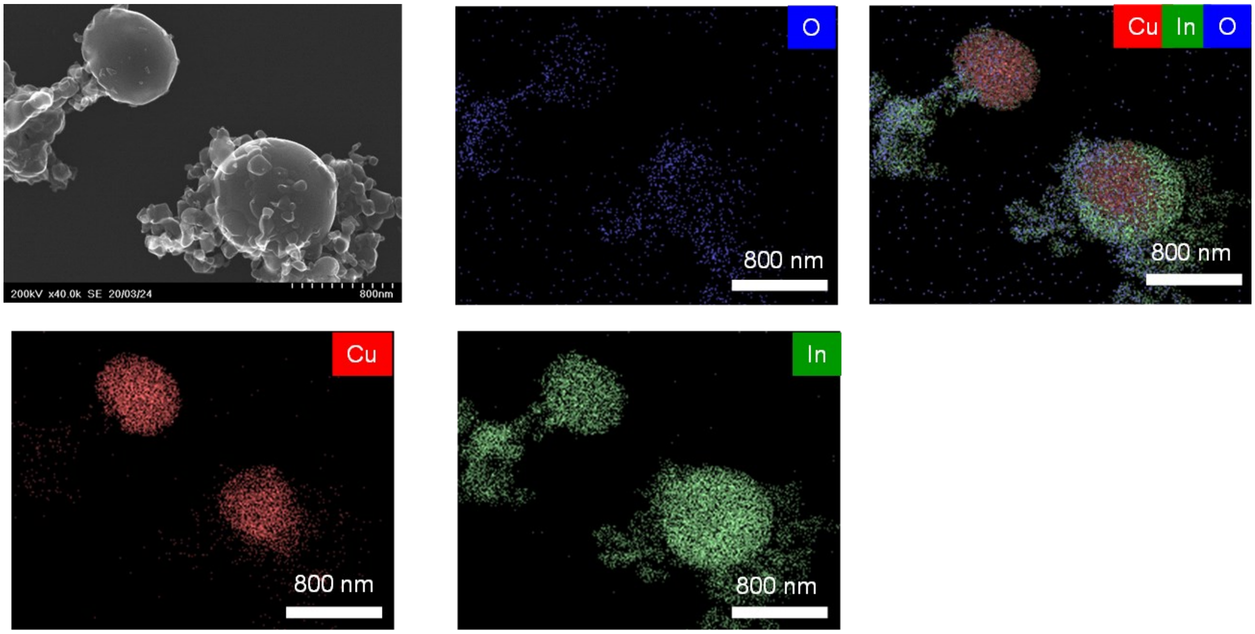

Fig. S11.

STEM-EDX images for 10wt% Cu/In_2O_3 after reduction at 773 K.

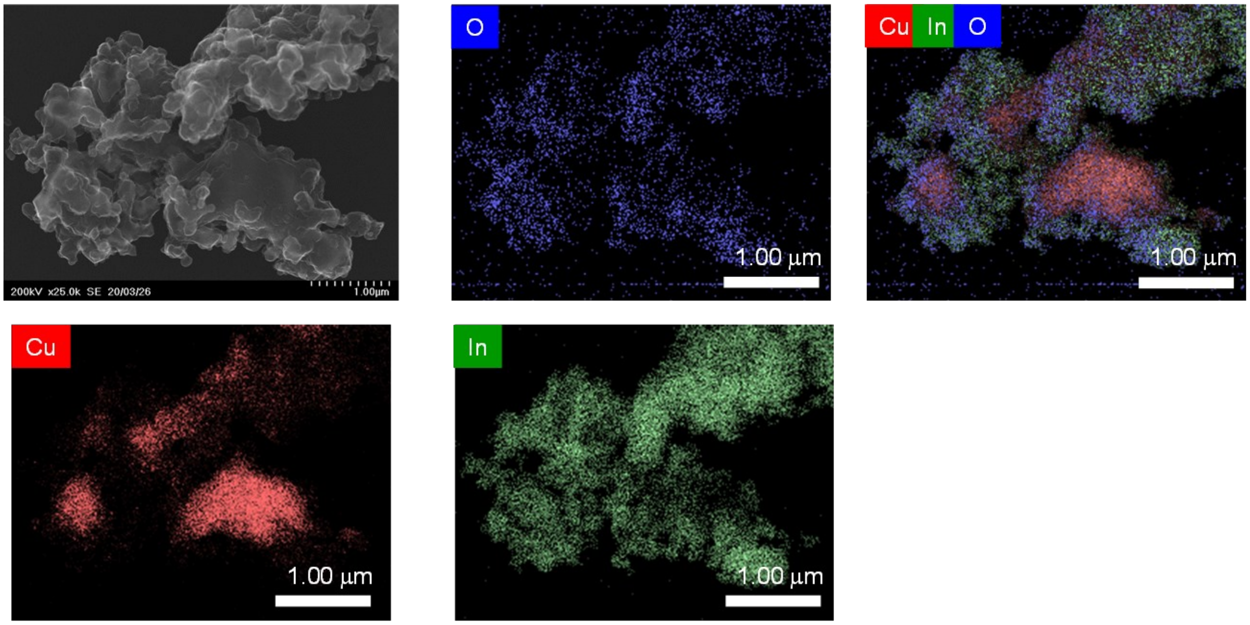

Fig. S12.

STEM-EDX images for 10wt% Cu/In_2O_3 after oxidation at 773 K.

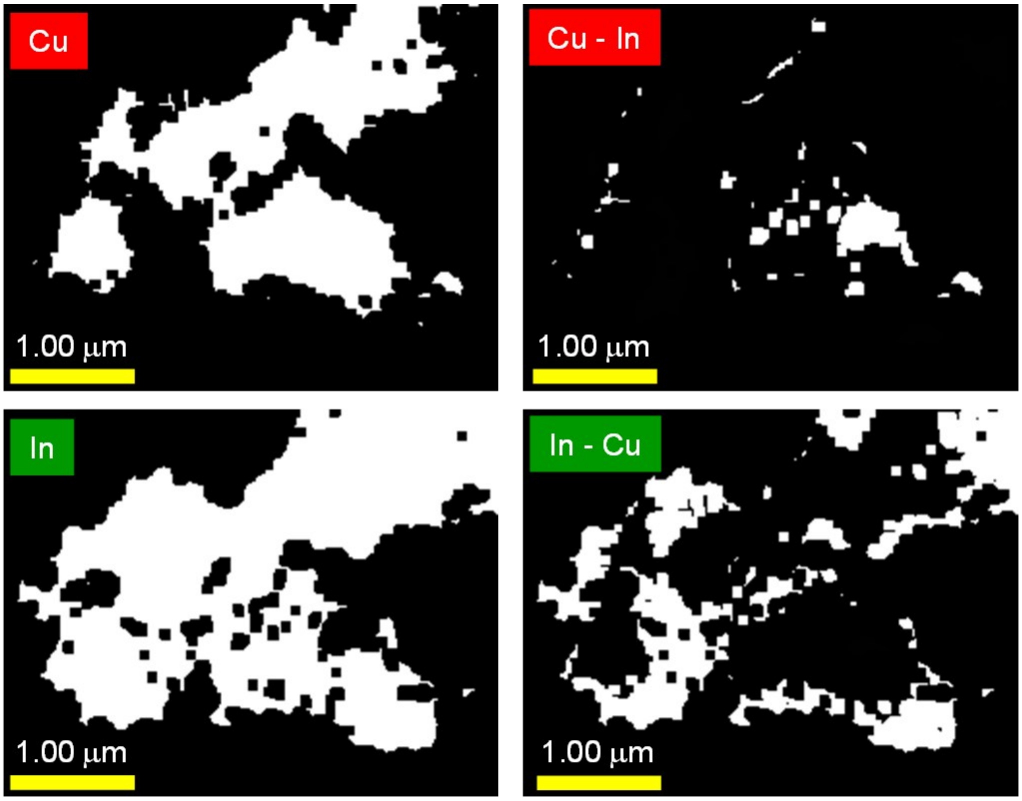

Fig. S13.

Binarized EDX mapping images for 10wt%Cu/In_2O_3 after oxidation at 773 K.

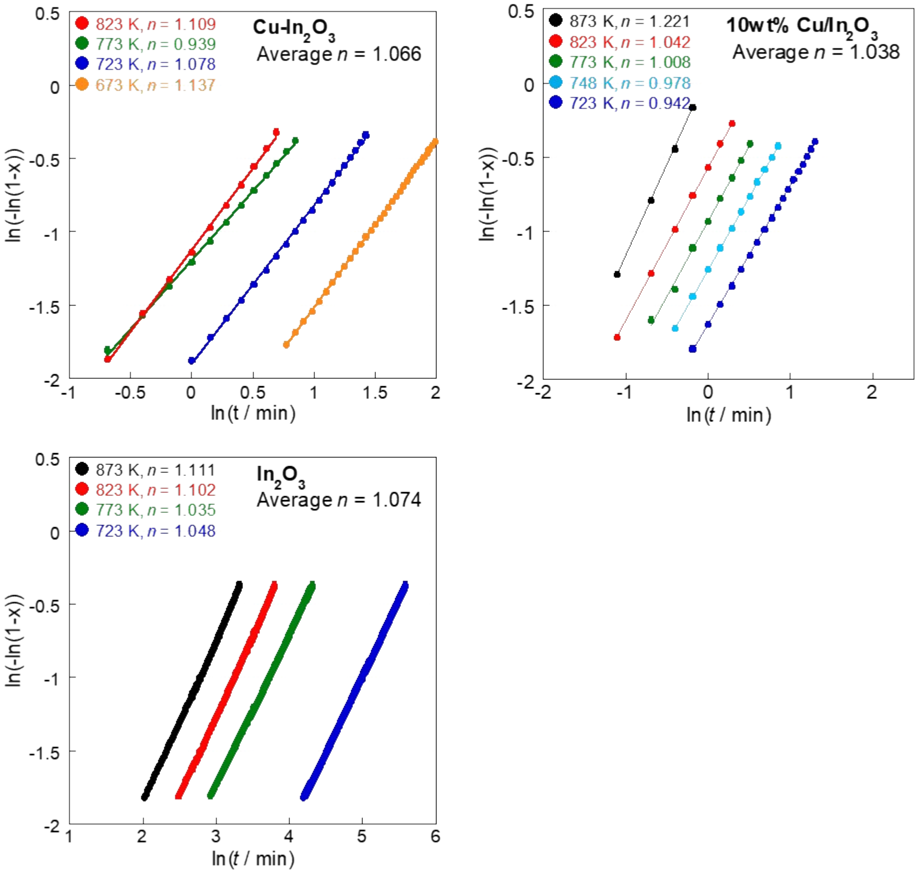

Fig. S14.

Plots of ln(−ln(1−x)) vs. ln(*t*) for the reduction of Cu-In_2O_3, 10wt% Cu/In_2O_3 and pure In_2O_3 by H_2.

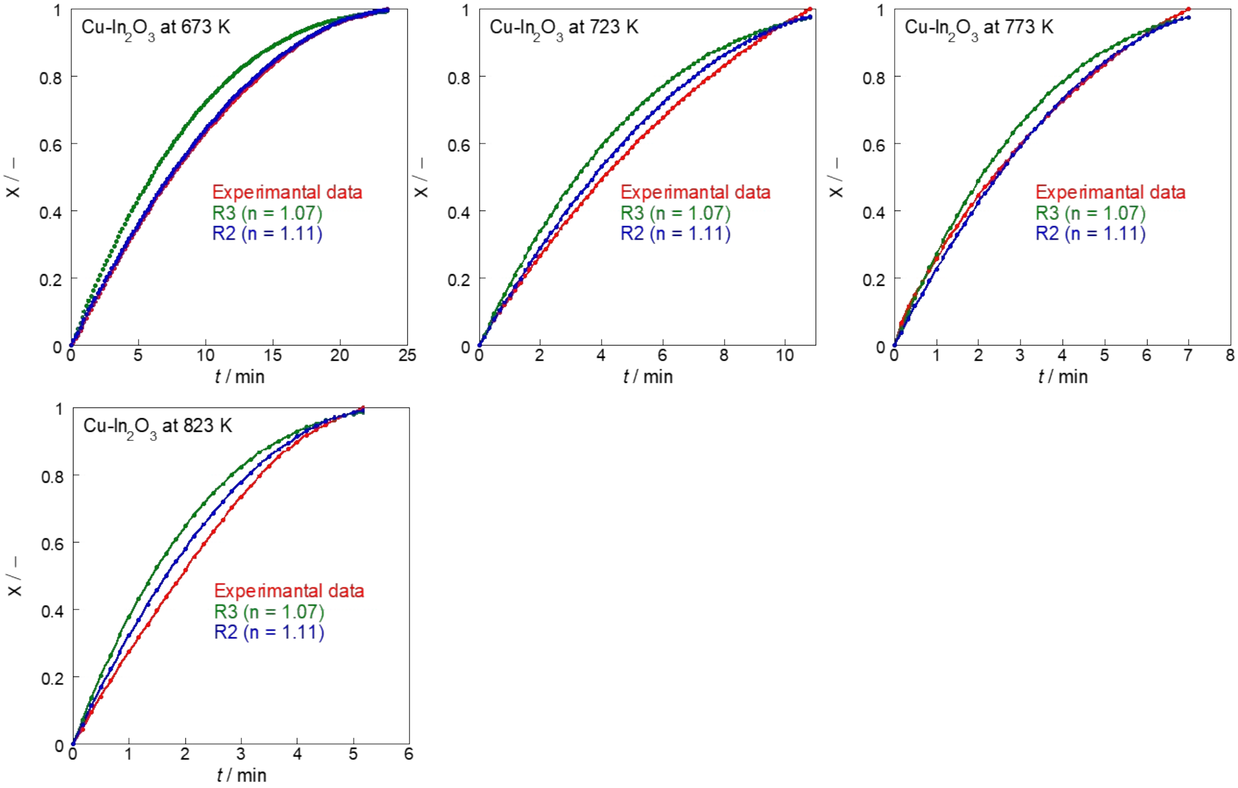

Fig. S15.

Comparison of experimental data for reduction of Cu-In_2O_3 by H_2 with Phase-boundary controlled reaction model (R2 and R3).

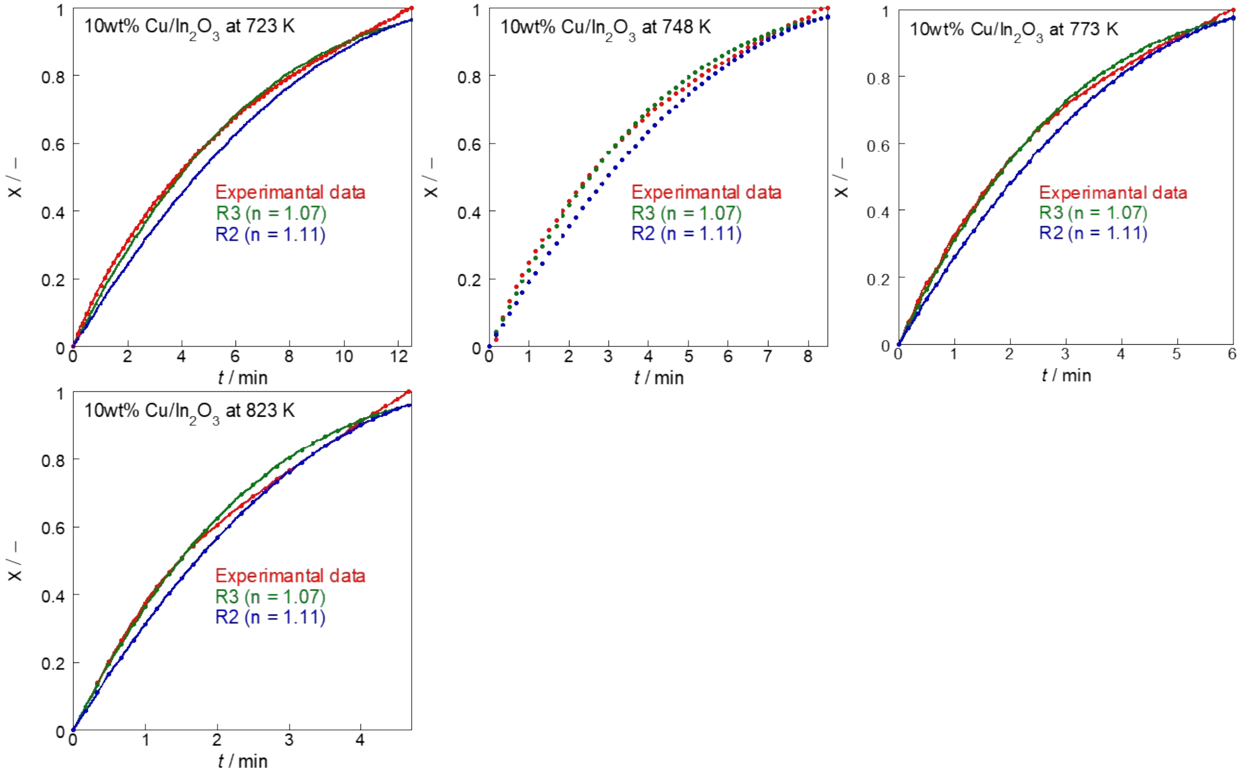

Fig. S16.

Comparison of experimental data for reduction of 10wt% Cu/In_2O_3 by H_2 with Phase-boundary controlled reaction model (R2 and R3).

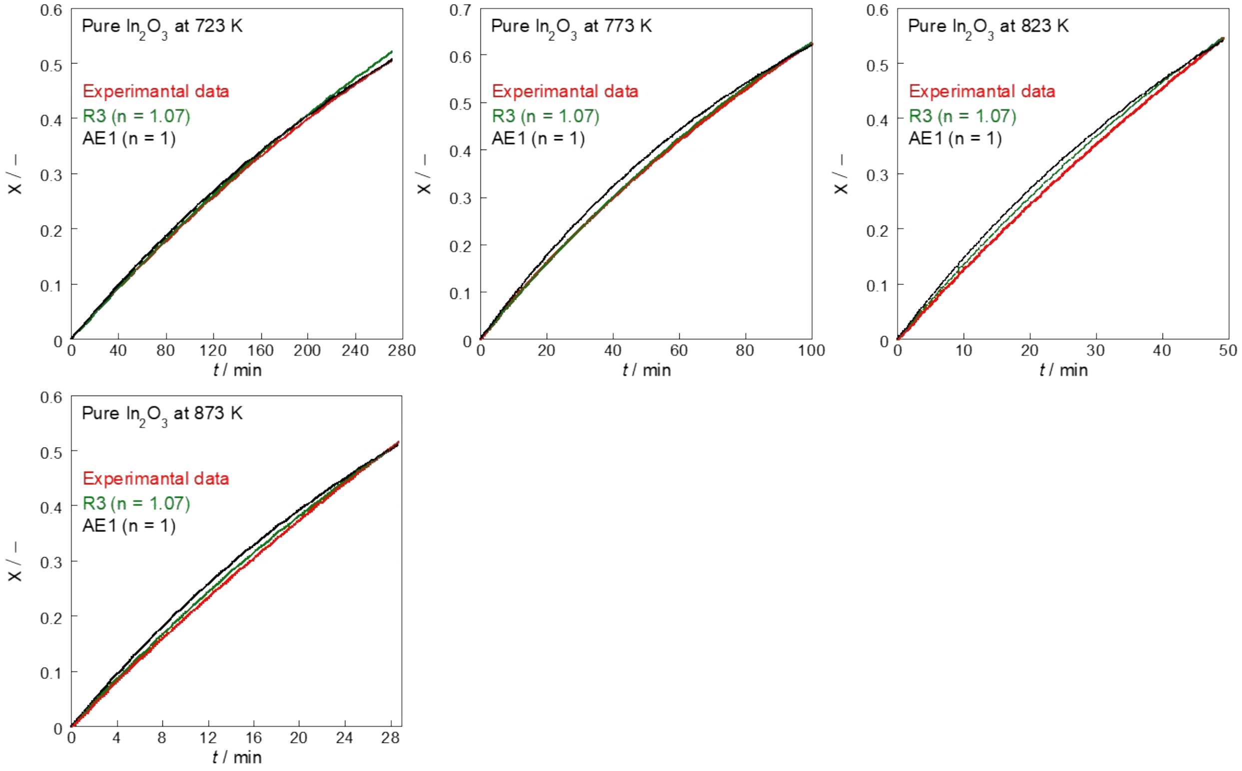

Fig. S17.

Comparison of experimental data for reduction of pure In_2O_3 by H_2 with Avrami-Erofe'ev model (AE1) and Phase-boundary controlled reaction model (R3).

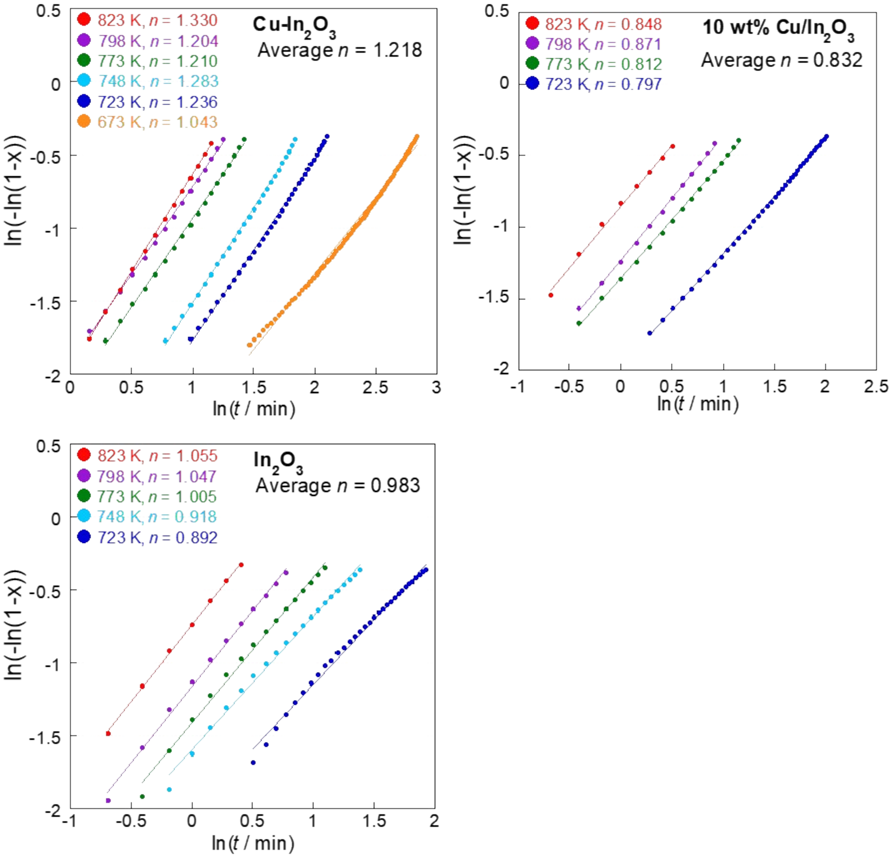

Fig. S18.

Plots of ln(−ln(1−x)) vs. ln(*t*) for the oxidation of Cu-In$_2$O$_3$, 10wt% Cu/In$_2$O$_3$ and pure In$_2$O$_3$ by CO$_2$.

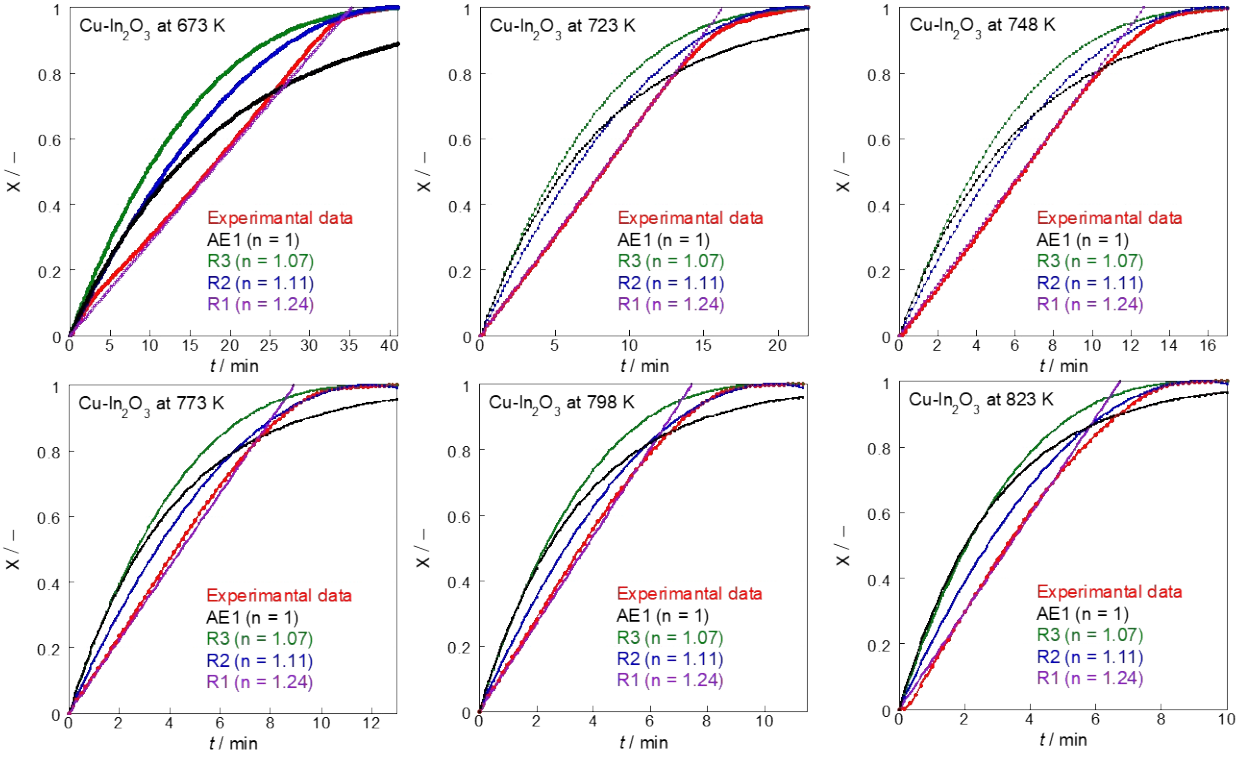

Fig. S19.

Comparison of experimental data for oxidation of Cu-In$_2$O$_3$ by CO$_2$ with Avrami-Erofe'ev model (AE1), Zero order reaction model (R1) and Phase-boundary controlled reaction model (R2 and R3).

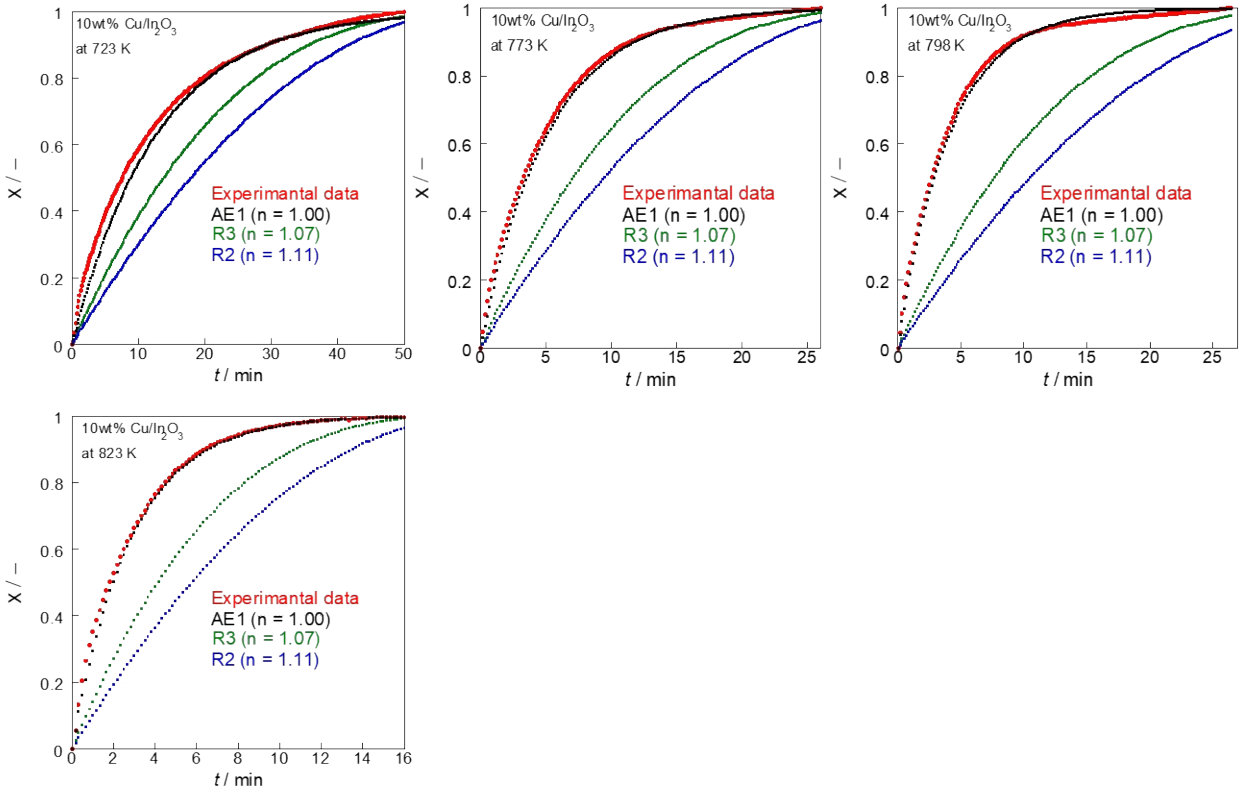

Fig. S20.

Comparison of experimental data for oxidation of 10wt% Cu/In_2O_3 by CO_2 with Avrami-Erofe'ev model (AE1) and Phase-boundary controlled reaction model (R2 and R3).

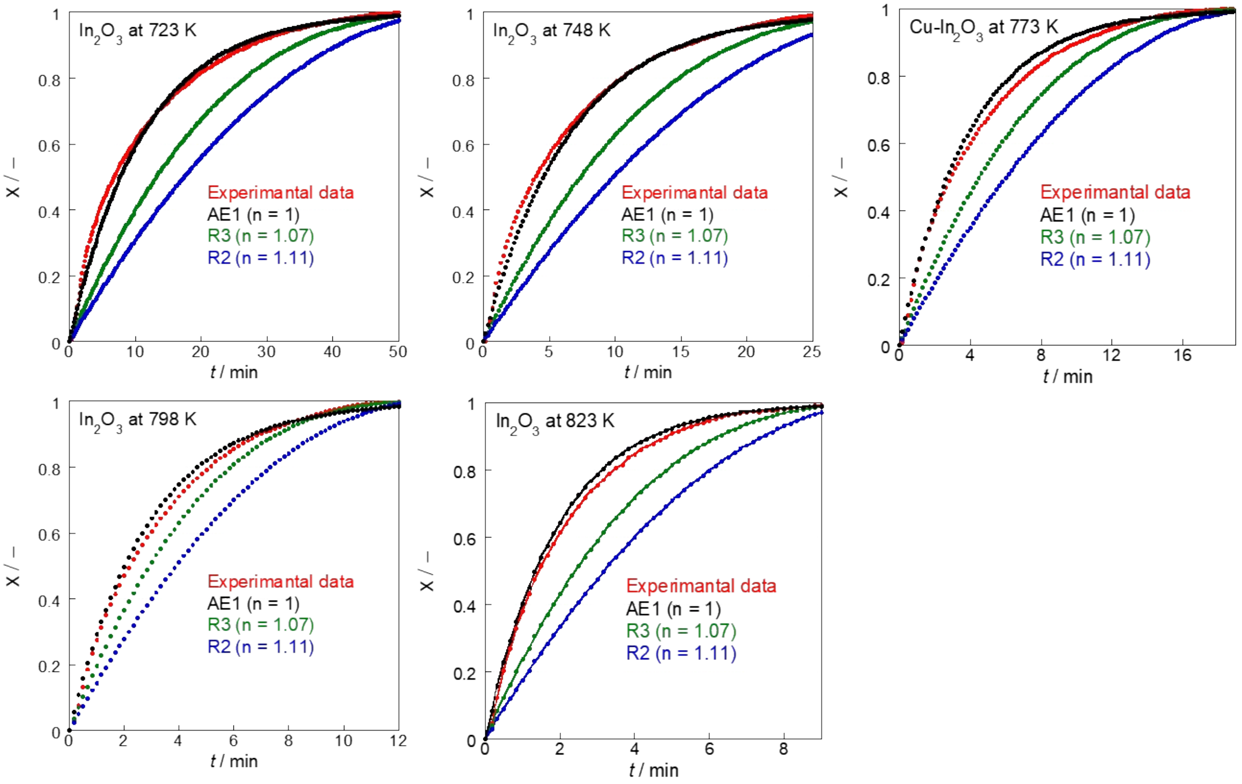

Fig. S21.

Comparison of experimental data for pure In_2O_3 with Avrami-Erofe'ev model Phase-boundary controlled reaction model (R2 and R3).

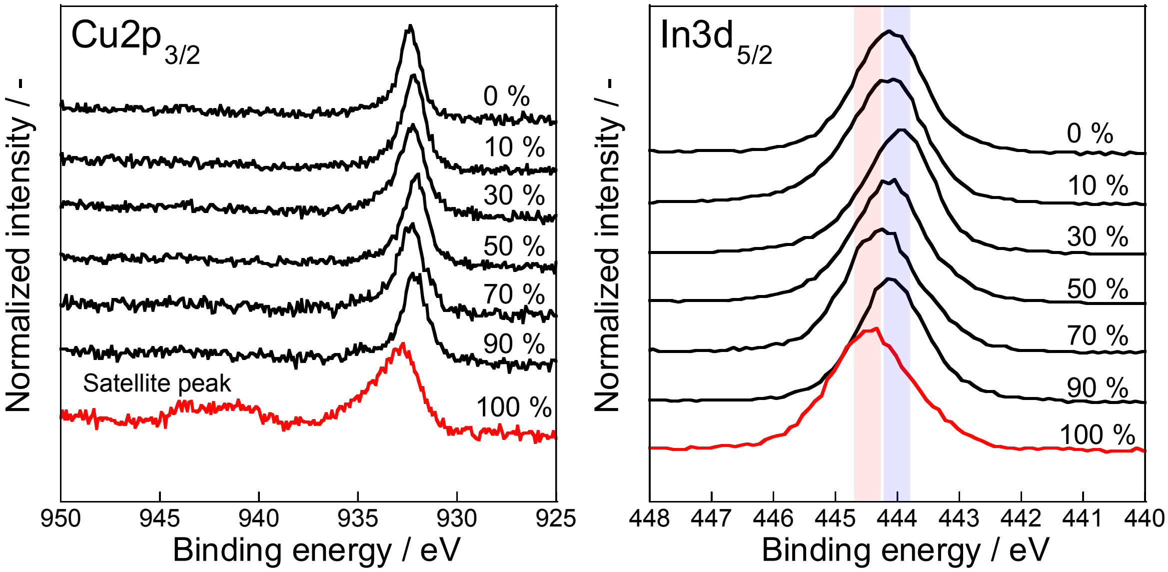

Fig. S22.

XPS spectra of Cu2p$_{3/2}$ and In3d$_{5/2}$ for Cu-In$_2$O$_3$ with various re-oxidation rate.

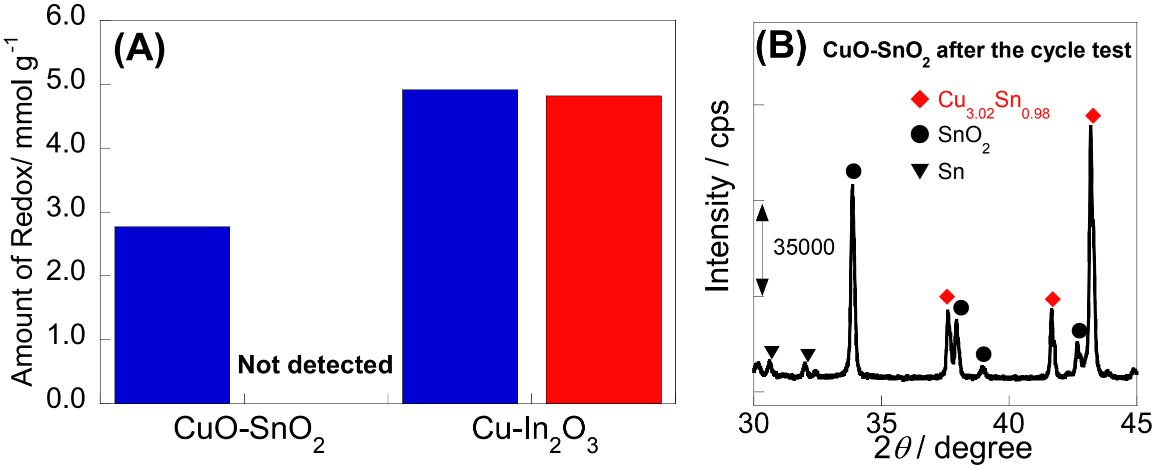

Fig. 23.

Isothermal RWGS-CL performance on CuO-SnO$_2$ at 773 K. (A) The performance of CuO-SnO$_2$ for RWGS-CL and (B) the XRD pattern of CuO-SnO$_2$ after the RWGS-CL cycle test.

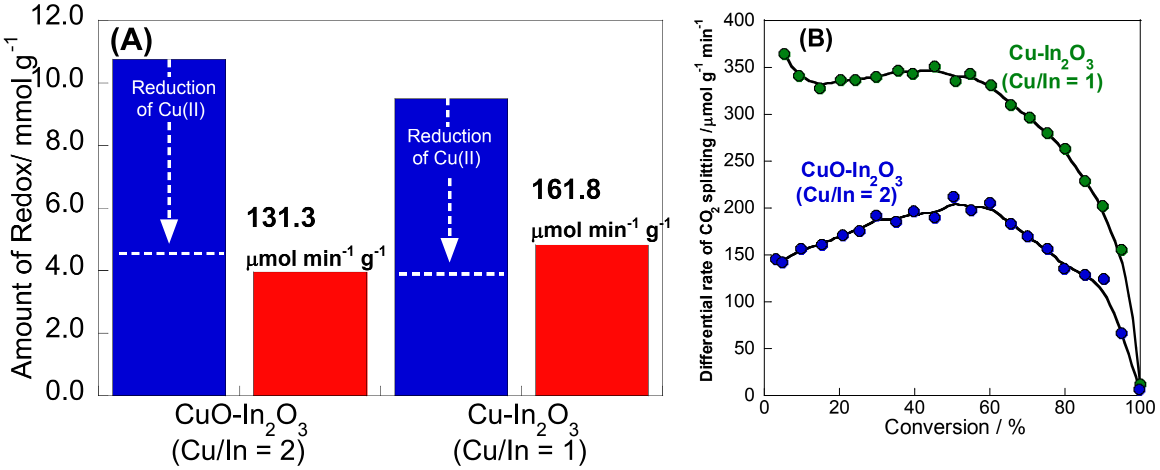

Fig. 24.

Isothermal RWGS-CL performance on CuO-In$_2$O$_3$ (Cu/In = 1) at 773 K. (A) Amounts of redox and average CO$_2$ splitting rate during re-oxidation step and (B) dependence of differential CO$_2$ splitting rate on conversion of oxides.

Table. S1.

Comparison of the CO_2 splitting performance at low temperature range with the various oxides in previous reports.

Material	Oxidation temperature / K	Partial pressure of CO_2 / %	CO_2 splitting amount /mmol g^{-1}	CO_2 splitting rate /μmol g^{-1} min^{-1}	Reference
$La_{0.75}Sr_{0.25}FeO_3$	823	6.7	4.00	73.1	(*14*)
$La_{0.6}Ca_{0.4}Fe_{0.4}Mn_{0.6}O_3$	823	10	0.973	160	(*15*)
$Mn_{0.2}Co_{0.8}Fe_2O_4$	923	20	8.8	142.3	(*16*)
$Cu_{0.4}Co_{0.6}Fe_2O_4$	823	20	-	98.3	(*17*)
	923	20	9.10	144.6	
In_2O_3	673	10	0.46	17.4	This work
	723	10	1.11	37.2	
	773	10	1.64	93.4	
10 wt% Cu/In_2O_3	673	10	0.45	3.5	This work
	723	10	1.60	28.5	
	773	10	2.79	117.0	
$Cu\text{-}In_2O_3$	673	10	2.90	58.7	This work
	723	10	3.79	115.0	
	773	10	4.80 ± 0.40	161.8 (1st cycle) 85.5 (5th cycle)	

Table S2.

Surface area of Cu-In_2O_3 (as-prepared and post-reaction) and previous reported OSMs.

Material		BET surface area / $m^2\ g^{-1}$	Reference
$La_{0.75}Sr_{0.25}Co_{(1-Y)}Fe_YO_3$		0.41–1.32	*(14)*
Fe-substituted Ba-hexa-aluminate		2–30	*(19)*
Cu-In_2O_3	as-prepared ($Cu_2In_2O_5$)	4.5	This work
	After reaction at 773 K(1st cycle)	3.2	This work
	After reaction at 773 K(3rd cycle)	0.8	This work

Table S3.

Relationship between the surface area and CO_2 splitting rate on Cu-In_2O_3.

Material	BET surface area / $m^2 g^{-1}$	Average CO_2 splitting rate **per gram of Cu-In_2O_3** / $\mu mol\ g^{-1}\ min^{-1}$	Average CO_2 splitting rate **per unit surface area of Cu-In_2O_3** / $\mu mol\ m^{-2}\ min^{-1}$
$Cu_2In_2O_5$ (As made)	4.5	-	-
Cu-In_2O_3 (1st cycle)	3.2	161.8	35.9
Cu-In_2O_3 (2nd cycle)	2.1	115.6	36.1
Cu-In_2O_3 (3rd cycle)	0.8	93.0	44.3
Cu-In_2O_3 (4th cycle)	-	86.0	107.5

Table S4.

Ratio of In(0) during the reduction and the oxidation at 773 K, as estimated by linear combination fitting of In *K*-edge spectra.

Time / min	Ratio of In (0) during reduction step / %	Ratio of In (0) during oxidation step / %
10	28.5	48.7
20	41.8	33.6
30	49.3	20.4
40	-	6.7
50	-	2.8
60	-	1.9

Table S5.

Rate equations and n values for various solid-state reaction models.

Function	Reaction model	Equation	n
D1	One-dimensional diffusion	$x^2 = kt$	0.62
D2	Two-dimensional diffusion Valensi equation	$(1-x)\ln(1-x) + x = kt$	0.57
D3	Three-dimensional diffusion Jander equation	$[1-(1-x)^{1/3}]^2 = kt$	0.54
AE1	Avrami-Erofe'ev (n = 1)	$-\ln(1-x) = kt$	1
AE3	Avrami-Erofe'ev (n = 3)	$-\ln(1-x)^{1/3} = kt$	3
R1	Zero order reaction	$x = kt$	1.24
R2	Phase-boundary-controlled reaction (contracting area)	$1- (1-x)^{1/2} = kt$	1.11
R3	Phase-boundary-controlled reaction (contracting volume)	$1- (1-x)^{1/3} = kt$	1.07

Table S6.

Root-mean square deviation to compare calculation conversion and experimental conversion for the reduction of Cu-In_2O_3.

Temperature / K	Root Mean Square Deviation	
	R3	R2
673	0.0620	0.0076
723	0.0709	0.0296
773	0.0406	0.0056
823	0.0840	0.0406

Table S7.

Root-mean square deviation to compare calculation conversion and experimental conversion for the reduction of 10wt% Cu/In_2O_3.

Temperature / K	Root Mean Square Deviation	
	R3	R2
723	0.0166	0.0470
748	0.0132	0.0377
773	0.0101	0.0322
823	0.0188	0.0554

Table S8.

Root-mean square deviation to compare calculation conversion and experimental conversion for the reduction of In_2O_3.

Temperature / K	Root Mean Square Deviation	
	R3	AE1
723	0.0068	0.0076
773	0.0029	0.0157
823	0.0100	0.0197
873	0.0070	0.0173

Table S9.
Reaction rate constant *k* values for reduction of oxides by H_2.

Oxide	Kinetic model	Reaction rate constant *k* / 10^{-1} min^{-1}					
		673 K	723 K	748 K	773 K	823 K	873 K
Cu-In_2O_3	R2	0.402	0.785	-	1.203	1.763	-
10wt% Cu/In_2O_3	R3	-	0.529	0.820	1.166	1.574	-
In_2O_3	R3	-	0.008	-	0.028	0.047	0.074

Table S10.

Root-mean square deviation to compare the calculation conversion and the experimental conversion for the oxidation of Cu-In_2O_3.

Temperature / K	Root Mean Square Deviation			
	R2	R1	R2 ($x < 0.8$)	R1 ($x < 0.8$)
673	0.1050	0.0435	0.1263	0.0178
723	0.0773	0.1144	0.0950	0.0058
748	0.0838	0.1253	0.1041	0.0130
773	0.0511	0.1560	0.0686	0.0190
798	0.0427	0.1865	0.0576	0.0149
823	0.0597	0.1728	0.0779	0.0149

Table S11.

Root-mean square deviation to compare the calculation conversion and the experimental conversion for the oxidation of 10wt% Cu/In_2O_3.

Temperature / K	Root Mean Square Deviation
	AE1
723	0.0297
773	0.0178
798	0.0167
823	0.0158

Table S12.

Root-mean square deviation to compare the calculation conversion and the experimental conversion for the oxidation of In_2O_3.

Temperature / K	Root Mean Square Deviation
	AE1
723	0.0230
748	0.0221
773	0.0252
798	0.0220
823	0.0206

Table S13.

Reaction rate constant *k* values for oxidation of oxides by CO_2.

Oxide	Kinetic model	Reaction rate constant k / 10^{-1} min^{-1}					
		673 K	723 K	748 K	773 K	798 K	823 K
Cu-In_2O_3	R1	0.284	0.614	0.789	0.956	1.307	1.456
10wt% Cu/In_2O_3	AE1	-	0.785	-	1.944	2.443	3.505
In_2O_3	AE1	-	0.894	1.526	2.549	3.438	5.147

Reference

32. M. Chen, J. Xu, Y.-M. Liu, Y. Cao, H.-Y. He, J.-H. Zhuang, Supported indium oxide as novel efficient catalysts for dehydrogenation of propane with carbon dioxide. *Appl. Catal., A* **1377**, 35–41 (2010).
33. Y.J. Jang, J. Lee, J.H. Kim, B.J Lee and J.S. Lee, One-dimensional CuIn alloy nanowires as a robust and efficient electrocatalyst for selective CO_2-to-CO conversion. J. Power Sources **378**, 412-417 (2018).